Stroboscopic imaging system for studying the dynamics of superconducting levitation bearings

Adrian Voß, James G. Storey, *Member, IEEE*, Luke Porteous, Patrick Scheunemann and Rodney A. Badcock *Senior Member, IEEE*

Abstract—Passively stable contactless high-speed bearings based on a magnetic rotor levitating above a high-temperature superconductor are desirable for many applications. Understanding the dynamics of spinning superconducting bearings is critical to their design, however, motion blur in video footage makes it difficult to analyse vibrations, oscillations and precession. Here we present a cost-effective stroboscopic imaging system synchronised with the rotor frequency. This makes the rotor appear frozen about the axis of spin, allowing changes in rotor position and tilt angle to be clearly observed. Position and orientation is automatically determined by computer vision tracking of an ArUco marker attached to the rotor. A trial of the system in a spin-down experiment shows that it is able to capture all six degrees of freedom of the rotor during its decoupling from the drive shaft at 6000 rpm. To our knowledge, this marks the first use of the stroboscopic method applied to the study of superconducting bearings.

Index Terms—Superconducting magnetic bearing, stroboscope, ArUco, fiducial marker

I. INTRODUCTION

THE inherently low stiffness of superconducting magnetic levitation bearings [1], [2] makes understanding their dynamic properties critical to their design. Mechanical perturbations, resonances, magnetic field variations and cryogenic system failures can lead to oscillations, vibrations, precession, and levitation height decay of the rotor [3], [4]. Positional information can be measured by eddy current sensors [5], lasers [6]–[8], Hall sensors [9] and capacitive sensors [10]. These are sensitive to μm-scale displacements and can operate at high frequencies, but a separate sensor is needed for each axis and it is difficult to determine changes in orientation of the rotor.

Imaging the rotor is desirable, however, capturing clear images of a rapidly spinning body ordinarily requires an expensive fast shutter speed camera to avoid motion blur. An alternative is to harness the stroboscopic effect where a rotating or oscillating object appears frozen when illuminated by a strobing light source that is matched to the frequency of the object [11]. Here the exposure time is determined
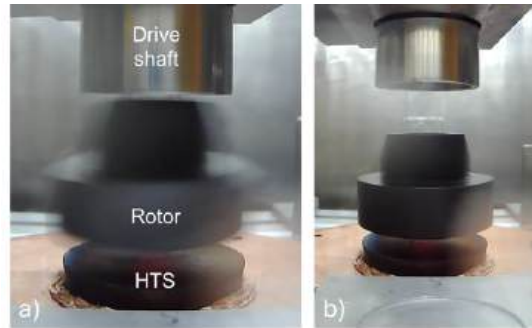
Fig. 1. Video frames captured with a 60 fps camera during a 6000 rpm superconducting levitation spin-down experiment, (a) directly after release from the drive shaft, and (b) at a later time when stable rotation has been reached.

by the light source rather than the shutter speed, allowing a lower speed camera to be used. Stroboscopes are commonly used in industry to visually inspect rotating machinery during operation, eliminating down-time. For a rotor speed of 6000 rpm (10 ms period), limiting the allowed rotor movement to 1 pixel in an image 1920 pixels wide requires a maximum strobe pulse duration of 2.6 μs.

Here we detail a cost-effective stroboscopic imaging system incorporating computer vision *pose* detection retrofitted into an spinning levitation bearing test rig. Results are then presented from a trial spin-down experiment, demonstrating that the system is capable of revealing all six degrees of freedom of the rotor throughout its decoupling from the drive shaft. To our knowledge, this marks the first use of the stroboscopic method applied to the study of superconducting bearings.

II. EXPERIMENTAL DETAILS

A. Test rig

The test rig improved upon in this work was originally developed to undertake spin-down studies to study the ac loss of high-speed superconducting levitation bearings [7], [12]. The setup, housed inside a vacuum cryostat, operates as follows. A rotor, comprising a permanent magnet (17 mm diameter 10 mm thick cylindrical N45-grade NdFeB magnet) bonded inside a plastic holder (Fig. 2(c)), is field-cooled a short distance (typically a few mm) above a 28 mm diameter 10 mm thick cylindrical GdBCO HTS bulk from CAN Superconductors [13] which is cryo-cooled via a Coolstar 0/40 cold head of a GM cryocooler supplied by Oxford Cryosystems [14]. The top of the magnet holder couples to a drive shaft and motor attached to a vertical translation stage [7], [12]. The
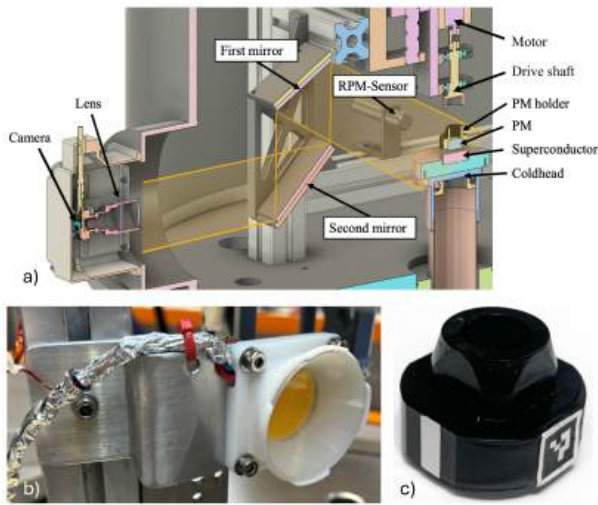
Fig. 2. (a) Cutaway drawing of the test rig showing the periscope mirror arrangement for increasing the camera's angle of view of the levitating permanent magnet (PM). (b) Photograph of the LED and reflector mounted inside the test rig. (c) Photograph of the permanent magnet holder featuring flat surfaces with a 10 × 10 mm ArUco marker glued on the right side. The reflective strip on the left side triggers the LED to flash once per rotation.

Fig. 3. Electrical power consumed during a 2 μs flash of the LED.

motor spins the rotor up to the desired speed at which point the linear stage moves the drive mechanism upwards leaving the levitating rotor spinning freely above the superconductor.

Rotation speed is measured by a Monarch Instrument ROS-W remote optical LED sensor [15] which detects light reflected from a silver strip on the magnet holder. Video of the experiments is captured by an inexpensive webcam mounted inside the cryostat, taking care to ensure a conduction cooling path to the cryostat room temperature wall. Example frames are shown in Fig. 1 and the full video is available at [16]. Limited *1-D* information about the levitation height was originally provided by a Keyence IB-30 thrubeam-type laser detection sensor [17] mounted to the windows of the cryostat.

B. Camera and optics

In this work, the laser displacement sensor is replaced by a monochrome Basler dart daA1440-220um/c 1440 x 1080 pixel industrial area scan camera [18]. It features a frame rate of 227 fps, a global shutter, and can by synchronised by software or hardware triggers. Here a LabVIEW control program updates exposure time every 100 ms based on the measured rotor speed. When an image is taken, the measurement time in millisecond resolution is included in the file name. The camera is connected to a *5 megapixel* 5-50mm 1/2.7 inch varifocal M12 mount lens with IR filter, manual focus and zoom. Camera and lens are mounted in front of a cryostat window, surrounded by an enclosure to block stray light, see Fig. 2(a). The camera views the rotor via a periscope mirror setup which increases the angle of view, important for the computer vision pose estimation system described below in section II-D.

C. Strobe light

The strobe light is adapted from a system originally developed for imaging aerosol nucleation [19]. The light source
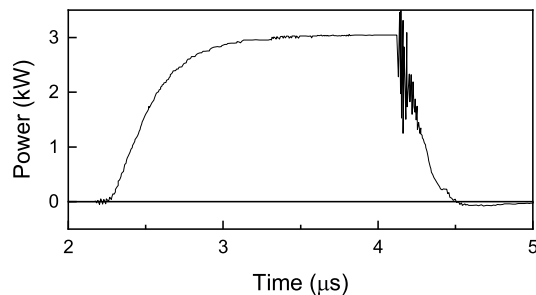
is a Cree XLamp® CXB3590 LED [20]. It is mounted on an aluminium sheet metal arm, which when bolted to the internal frame of the test rig provides sufficient heat sinking to the ambient cryostat wall in vacuum. A white *3-D*-printed polylactic acid (PLA) reflector with a protective plexiglass window is attached over the LED, see Fig. 2(b).

A custom flash driver circuit is controlled by an Arduino Nano Every board based on the ATMega4809 microcontroller with a clock speed of 20 MHz [21]. When the Arduino receives a rising edge from the rpm sensor it switches an Infineon IPP60R190P6 power MOSFET [22] which releases the charge stored in a 50 μF 200 V capacitor to the LED. To achieve the necessary speed and precision, the timing of the switching function is implemented in assembly language embedded inline using the `asm volatile` directive. The capacitor is charged between flashes via an integrated step-up converter delivering 125 V output from 12 V input. Pulse duration is set in the LabVIEW program and communicated to the board via the Arduino's [21] USB serial connection. The program also monitors the LED temperature and deactivates flashing if the temperature rises above a user-specified limit.

Oscilloscope measurements show that a flash is activated approximately 3 μs after receipt of the input trigger, corresponding to a negligible 0.1° rotation of the rotor at 6000 rpm. Maximum voltage and current applied to the LED are 107 V and 28 A respectively. The power consumed by the LED during a 2 μs pulse, shown in Fig. 3, peaks at 3045 W. This is some 35 times higher than the rated 86 W continuous output power of the LED. However, due to the very short duty cycle, the average power dissipation while operating at 100 Hz is only 517 mW.

D. Computer vision pose estimation

Clear images produced by the camera and strobe light allow the position and orientation of the rotor to be automatically extracted by computer vision. This was achieved by attaching a fiducial marker [23] to the rotor. Such markers are commonly used for extracting camera pose in augmented reality applications. Alternatively when the camera position is known, they can be used to determine the position and orientation of an object in space. This method is reliable and accurate and robust to slight changes in viewing perspective. The ArUco marker [24] was selected, which offers good performance and is supported by the OpenCV library [25]. The marker must be placed on a flat surface, so a new PM
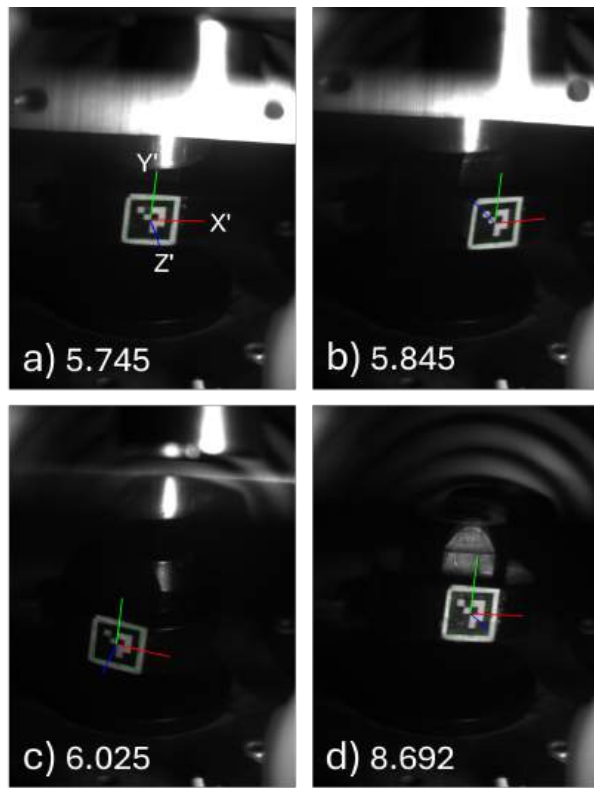
Fig. 4. Processed frames captured at selected times during a spin-down experiment as the rotor is released at 6000 rpm. The green tracking box and local coordinate axes are overlaid by the ArUco marker detection algorithm. A flipping of the Z'-axis is visible in (b).

holder with 4 flat sides was milled with a CNC machine from Acetal (polyoxymethylene or POM) plastic, see Fig 2(c). To improve measurement accuracy a periscope mirror setup was incorporated into the cryostat to shift the viewing angle of the camera so that it is not perpendicular to the marker [23]. In the setup, shown in Fig. 2(a), the angle of view is 27° from the horizontal.

III. TEST RESULTS

The imaging system was tested in the following spin-down experiment. A 28 mm diameter 10 mm thick cylindrical GdBCO HTS bulk from CAN Superconductors [13] was field-cooled to 50 K with a 17 mm diameter 10 mm thick cylindrical N45-grade NdFeB magnet located above it at a distance of 9.5 mm. The relatively large distance was chosen to reduce the stiffness and increase the amount of movement experienced by the rotor during release. The rotor was spun up to 6000 rpm and released. A total of 515 images were captured, successfully recording the decoupling process.

The images were post-processed with a python script to extract the pose information using the ArUco marker detection algorthim in OpenCV. The script outputs processed images which include a tracking box and local coordinate axis (X', Y', Z') overlaid on the marker. Examples at selected times are shown in Fig. 4. A video of the full set of images is available at [26]. (The rotor is more clearly visible in footage of an earlier experiment that tested T-shaped tracking markers
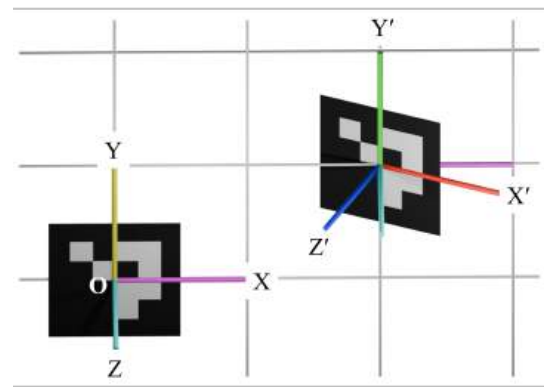

Fig. 5. The displacement and rotation of the marker are specified with respect to the initial position and orientation, shown by (X, Y, Z). Here the marker defined by axes (X', Y', Z') is displaced by two units in the X direction, one unit in the Y direction, and rotated by 25 degrees about the Y direction.

[27]). The machine vision algorithm successfully tracked the ArUco marker in almost all images. Only at the beginning, shortly after decoupling, were images taken where the marker tilted too much or there were unintentional double exposures. The decoupling process is less than ideal and the drive shaft can knock the rotor causing large initial movements. The blue Z'-axis (perpendicular to the marker) sometimes jumps in sign, but this can be easily corrected for in the script.

The script also outputs the time dependence of the six degrees of freedom to a data file. These consist of three displacements (ΔX, ΔY, ΔZ) and three rotations (Rot X, Rot Y, Rot Z), defined relative to the initial orientation of the marker (X, Y, Z) when the rotor was coupled to the drive shaft, see Fig. 5. The six degrees of freedom are are plotted in Fig. 6(a) – (f). Note that the Z-displacement (d) is not yet calibrated, and an extra transformation is needed to shift the origin from the marker to the centre of the magnet. Nevertheless, the data reveals a high frequency vibration immediately after release, lasting for approximately 3 seconds. These occur on a longer damped sinusoidal background oscillation which has a frequency of around 0.25 Hz. We define the nutation angle θ as

$$\theta = \arccos(\cos\alpha\cos\beta) \tag{1}$$

where α and β are rotations around the X and Z-directions of the initial marker coordinate system respectively. The nutation angle plotted in Fig. 6(g) decays from a maxiumum of 15° towards a constant value of 11° over approximately 9 s. The damping envelope has the form $10.9 \pm 4.1\exp[-(t - 7.55)/3.33]$. The rotor eventually settles into a stable rotation with a constant tilt angle. The vertical position of the marker is some 3.7 mm higher than the release position. Its possible that stiction is causing the rotor to be dragged upwards slightly during the release process. The video [26] also suggests that some of the increase could be due to the tilt of the rotor.

IV. CONCLUSIONS

A cost-effective stroboscopic imaging system was successfully implemented to study the dynamics of high-speed rotating superconducting levitation bearings. Use of a 2 μs
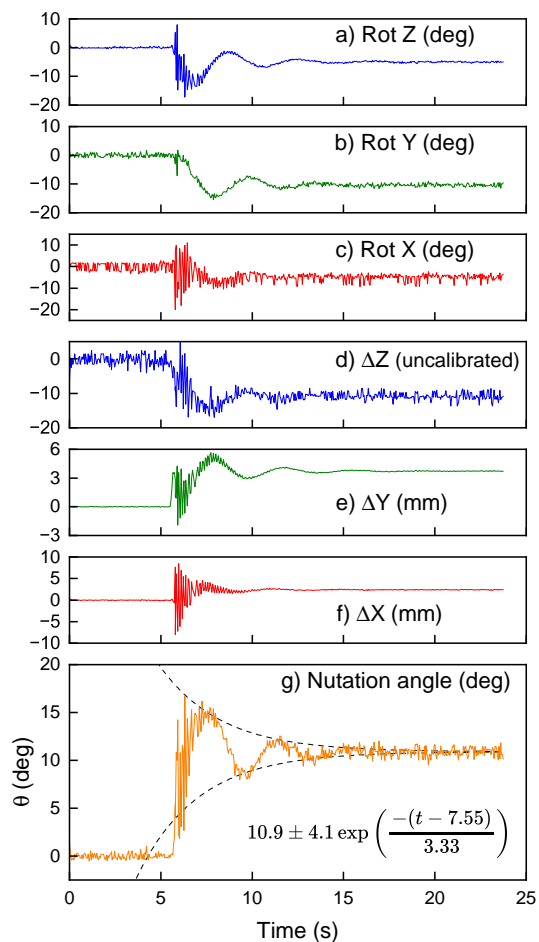
Fig. 6. (a) to (f) The six degrees of freedom extracted by the ArUco marker tracking algorithm during a spin-down experiment. (g) The nutation angle calculated from the angles in (a) and (c), and an exponential decay envelope (dashed lines).

strobe light eliminates motion blur, allowing clear images of the rotor to be captured at speeds tested up to 6000 rpm. Image clarity enables the pose of the rotor to be determined automatically by computer vision tracking of an ArUco marker attached to the side of the rotor. The system was tested on a spinning levitating rotor released at 6000 rpm. Both an initial high-frequency vibration and a longer damped oscillation were identifiable in the data. At present the system takes one image per rotation, capturing the same side of the rotor each time. The system could be improved by introducing a sliding delay between strobe pulses to capture images at different points in the rotation. This would enable vibrations with frequencies greater than the rotation frequency to be studied.

REFERENCES

[1] K. B. Ma, Y. V. Postrekhin, and W. K. Chu, "Superconductor and magnet levitation devices," *Review of Scientific Instruments*, vol. 74, no. 12, pp. 4989–5017, 12 2003, doi:10.1063/1.1622973.

[2] I. Valiente-Blanco, E. Diez-Jimenez, C. Cristache, M. A. Alvarez-Valenzuela, and J. L. Perez-Diaz, "Characterization and improvement of axial and radial stiffness of contactless thrust superconducting magnetic bearings," *Tribology Letters*, vol. 54, no. 3, pp. 213–220, Jun 2014, doi:10.1007/s11249-013-0204-0.

[3] A. Rastogi, A. Campbell, and T. Coombs, "Dynamics of superconductor bearings in a cryogenic failure," *Physica C: Superconductivity and its Applications*, vol. 442, no. 1, pp. 9–12, 2006, doi:10.1016/j.physc.2006.03.136.

[4] H. Liao, J. Zheng, L. Jin, H. Huang, Z. Deng, Y. Shi, D. Zhou, and D. A. Cardwell, "Dynamic levitation performance of Gd–Ba–Cu–O and Y–Ba–Cu–O bulk superconductors under a varying external magnetic field," *Superconductor Science and Technology*, vol. 31, no. 3, p. 035010, feb 2018, doi:10.1088/1361-6668/aaa82a.

[5] M. Komori, A. Tsuruta, S. Fukata, and T. Matsushita, "Static and dynamic characteristics of a superconducting bearing system using high t_c superconductors," in *Advances in Superconductivity VII*, K. Yamafuji and T. Morishita, Eds. Tokyo: Springer Japan, 1995, pp. 1289–1292, doi:10.1007/978-4-431-68535-7_293.

[6] M. Sparing, T. Espenhahn, G. Fuchs, M. Hossain, A. Abdkader, K. Nielsch, C. Cherif, and R. Hühne, "Analysis of the high-speed rotary motion of a superconducting magnetic bearing during ring spinning," *Engineering Research Express*, vol. 2, no. 3, p. 035039, sep 2020, doi:10.1088/2631-8695/abb7e4.

[7] M. Siamaki, J. G. Storey, L. Wiesehoefer, and R. A. Badcock, "Design, build, and evaluation of an AC loss measurement rig for high-speed superconducting bearings," *Energies*, vol. 15, no. 4, 2022, Art. no. 1427, doi:10.3390/en15041427.

[8] K. Yagi, R. Taniguchi, S. Ishida, and S. Ohashi, "Effects of the external vibrations on rotational stability of the HTS magnetic bearings," in *2023 IEEE International Magnetic Conference (INTERMAG)*, 2023, pp. 1–5, doi:10.1109/INTERMAG50591.2023.10265098.

[9] Y. Sakurai, T. Matsumura, H. Sugai, N. Katayama, H. Ohsaki, Y. Terao, Y. Terachi, H. Kataza, S. Utsunomiya, and R. Yamamoto, "Vibrational characteristics of a superconducting magnetic bearing employed for a prototype polarization modulator," *Journal of Physics: Conference Series*, vol. 871, no. 1, p. 012091, jul 2017, doi:10.1088/1742-6596/871/1/012091.

[10] S. Sugiyama, T. Ghigna, Y. Hoshino, N. Katayama, S. Katsuda, K. Komatsu, T. Matsumura, Y. Sakurai, K. Sato, R. Takaku, M. Tashiro, and Y. Terada, "Vibration characteristics of a continuously rotating superconducting magnetic bearing and potential influence to TES and SQUID," *Journal of Low Temperature Physics*, vol. 209, no. 5-6, p. 1088 – 1096, 2022, doi:10.1007/s10909-022-02846-1.

[11] Z. Ren, F. Fang, N. Yan, and Y. Wu, "State of the art in defect detection based on machine vision," *International Journal of Precision Engineering and Manufacturing - Green Technology*, vol. 9, no. 2, p. 661 – 691, 2022, doi:10.1007/s40684-021-00343-6.

[12] M. Siamaki, J. G. Storey, L. Wiesehoefer, and R. A. Badcock, "The impact of magnetic field periodicity on the hysteresis loss in superconducting magnetic bearings," *Superconductivity*, vol. 5, p. 100040, 2023, doi:10.1016/j.supcon.2023.100040.

[13] CAN Superconductors, https://www.can-superconductors.com/ Kamenice, Czech Republic, accessed Aug. 29, 2025.

[14] "Oxford Cryosystems Gifford McMahon Cryocoolers," accessed Sept. 10, 2025. [Online]. Available: https://oxcryo.com/app/uploads/2024/08/GM-Brochure-2025-v1.0-Digital-Version.pdf

[15] "ROS Remote Optical LED Sensor," Monarch Instrument, https://monarchinstrument.com/product/ros-remote-optical-led-sensor/, accessed Aug. 29, 2025.

[16] J. Storey and M. Siamaki, "Superconducting bearing spin-down experiment," 9 2025, doi:10.25455/wgtn.28012019, Accessed Sept. 10, 2025. [Online]. Available: https://openaccess.wgtn.ac.nz/articles/media/Superconducting_bearing_spin-down_experiment/28012019

[17] "Sensor Head – IB-30," Keyence, https://www.keyence.com/products/sensor/positioning/ib/models/ib-30/, accessed Aug. 29, 2025.

[18] "Basler dart daA1440-220um (S-Mount)," https://www.baslerweb.com/en-sg/shop/daa1440-220um-s-mount/, accessed Aug. 29, 2025.

[19] P. Scheunemann, M. Jermy, and P. Stephenson, "Cyclic appearance and disappearance of aerosol nucleation in the boundary layer of drops of volatile liquid," *Energies*, vol. 16, no. 22, 2023, doi:10.3390/en16227491.

[20] "XLamp® CXB3590 LED," Cree LED, https://downloads.cree-led.com/files/ds/x/XLamp-CXB3590.pdf, accessed Aug. 29, 2025.

[21] "Arduino Nano Every," https://store.arduino.cc/products/nano-every, accessed Aug. 29, 2025.

[22] "Infineon CoolMOS™ P6 PowerTransistor Datasheet," accessed Sept. 10, 2025. [Online]. Available: https://www.infineon.com/assets/row/public/documents/24/49/infineon-ipx60r190p6-ds-en.pdf

[23] M. Kalaitzakis, B. Cain, S. Carroll, A. Ambrosi, C. Whitehead, and N. Vitzilaios, "Fiducial markers for pose estimation: Overview, applications and experimental comparison of the artag, apriltag, aruco and

stag markers," *Journal of Intelligent and Robotic Systems: Theory and Applications*, vol. 101, no. 4, 2021, doi:10.1007/s10846-020-01307-9.

[24] S. Garrido-Jurado, R. Muñoz-Salinas, F. Madrid-Cuevas, and M. Marín-Jiménez, "Automatic generation and detection of highly reliable fiducial markers under occlusion," *Pattern Recognition*, vol. 47, no. 6, pp. 2280–2292, 2014, doi:10.1016/j.patcog.2014.01.005.

[25] G. Bradski, "The OpenCV Library," *Dr. Dobb's Journal of Software Tools*, 2000.

[26] J. Storey and A. Voß, "Stroboscopic images of a levitating rotor released at 6000 rpm on 28 January 2025." 9 2025, doi:10.25455/wgtn.30038278, Accessed Sept. 8, 2025. [Online]. Available: https://openaccess.wgtn.ac.nz/articles/media/Stroboscopic_images_of_a_levitating_rotor_released_at_6000_rpm_on_28_January_2025_/30038278

[27] ——, "Levitating rotor released at 6100 rpm imaged with a stroboscopic technique," 9 2025, doi:10.25455/wgtn.30132331, Accessed Sept. 16, 2025. [Online]. Available: https://openaccess.wgtn.ac.nz/articles/media/Levitating_rotor_released_at_6100_rpm_imaged_with_a_stroboscopic_technique/30132331